Korean J. Chem. Eng., 40(6), 1309-1316 (2023)
DOI: 10.1007/s11814-022-1329-3

pISSN: 0256-1115
eISSN: 1975-7220

Lattice Boltzmann modeling and analysis of ceramic filtration with different pore structures

Gi Wook Lee, Byoungjin Chun†, and Hyun Wook Jung†

Department of Chemical and Biological Engineering, Korea University, Seoul 02841, Korea
(*Received 1 October 2022 • Accepted 26 October 2022*)

Abstract−The pressure drop in the ceramic filter system of the after-treatment device has a great effect on automobile engine performance. To predict the pressure drop under various operating conditions, it is necessary to analyze how the structural properties of porous media affect the permeability. The commonly used Kozeny-Carman model correlating permeability and porosity is useful for porous media composed of spherical grains, but exhibits considerable deviations in the actual ceramic filter system with low porosity. In this study, the permeability of overlapped-random structured porous media with low porosity was numerically solved by mesoscopic lattice Boltzmann (LB) method in Darcy flow regime. Based on LB simulation results, a new capillary model modified from Kozeny-Carman model is proposed for practically predicting the permeability of complex porous filter systems, using key structural variables such as porosity, tortuosity, and effective pore-throat radius.

Keywords: Porous Media, Kozeny-Carman Equation, Permeability, Tortuosity, Pore Throat, Lattice Boltzmann Method

INTRODUCTION

Porous materials with intricate and tortuous internal structures have been used in various industrial fields such as for ceramic or membrane filters, battery electrodes, separator films, and drug delivery systems [1-6]. As environmental problems have recently emerged, various eco-friendly technologies using porous materials are increasingly attracting attention from researchers and engineers. Especially, a representative case to incorporate porous media is an engine particulate filter, i.e., diesel or gasoline particulate filter (DPF or GPF), which is an after-treatment device in the automobile industry. The DPF or GPF effectively removes particulate matter (PM) in the exhaust gas through a specialized-designed filtration process. The pressure drop during the filtration operation by the ceramic filter, due to the accumulation of PMs on or inside the filter, weakens the engine power of the vehicle. It is known that the pressure drop due to the deep bed filtration occurring in the voids and pores inside the filter during the initial filtration process accounts for a larger proportion than that caused by a soot layer formation on the saturated filter surface [7,8]. Therefore, to enhance automobile performance by reducing fuel consumption and PM/CO_2 emissions, it is very important to correctly predict the pressure drop of the ceramic filter during the initial filtration process by analyzing how the structural property of the porous media affects the flow characteristics through the filter wall.

A ceramic filter used as an after-treatment device is generally made of cordierite material by sintering Mg-Al silicate, having a porosity of 0.36 to 0.66 [9]. The exhaust gas emitted from the vehicle engine enters the inlet channel of the cordierite filter, passes through the filter wall, and exits the outlet channel, as schematically depicted in Fig. 1(a). The wall thickness (L_T) of cordierite filter is approximately 0.5 mm (Fig. 1(b)), where the filter wall consists of silicate particles approximately several μm in size (Fig. 1(c)). The flow speed of exhaust gas passing through the filter wall is typically about 0.1 m/s [10,11]. The kinematic viscosity of exhaust gas with low-concentrated PMs at the operating temperature of 300 °C or higher is approximately 5×10^{-5} m^2/s [12,13]. At small Reynolds number (Re) based on wall-flow velocity in filter estimated to be $\mathcal{O}(0.1)$, i.e., Darcy flow regime, the wall-flow velocity is linearly increased with pressure drop across the wall. However, note that the increase in engine temperature and power during temporal operating conditions can raise Re due to the decreased viscosity and increased filter wall-flow velocity, which exhibits nonlinear characteristics with wall-flow velocity increasing quadratically at Re>1, i.e., the non-Darcy flow regime as studied by Lee et al. [14].

Studies of porous media flows in the Darcy regime have been conducted in systems with various porous structures. Since the pioneering work by Kozeny and Carman, who identified the relationship between porosity and permeability for porous media by means of an empirical method [15,16], the ensuing numerical and theoretical studies have been expanded to more complex-structural cases with non-spherical ellipsoidal particles [17,18] or fibril geometry [19-21]. However, most ceramic materials constituting porous media are formed as particle composites, such as a ceramic filter rather than in the form of segmented individual particles (or grains), so that the permeability of a medium with realistic and intricate porous structures of low porosity does not always follow the predictions of the existing models [21-25].

In this study, mesoscopic flow simulation in porous media, especially under low porosity conditions, in the Darcy flow regime was performed to characterize the permeability in complicated porous media composed of nonoverlapped spherical particles or overlapped

†To whom correspondence should be addressed.
E-mail: bjchun@grtrkr.korea.ac.kr, hwjung@grtrkr.korea.ac.kr

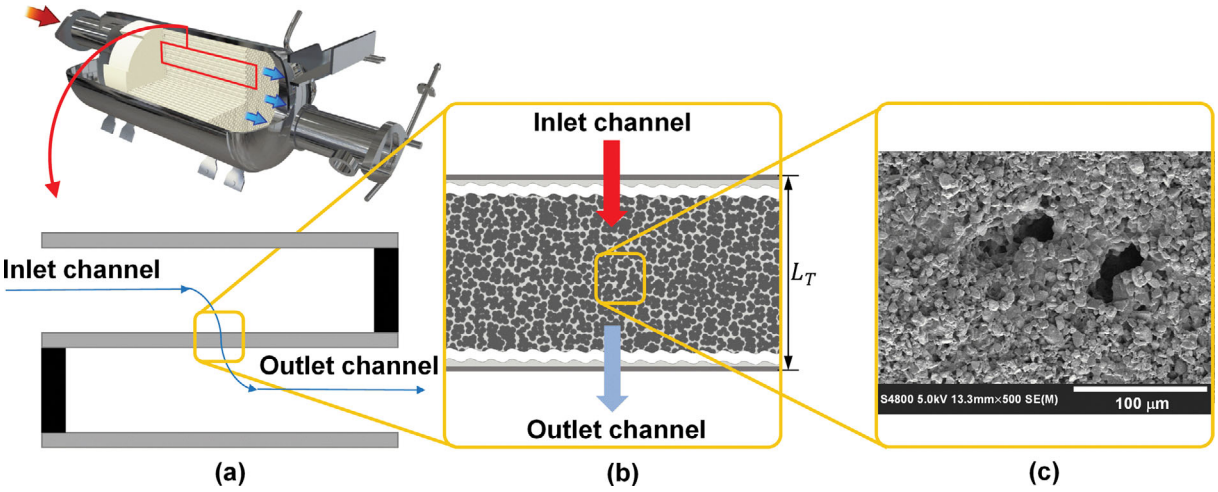

Fig. 1. (a) Schematic image of DPF/GPF system and the structure of filter channels with inlet and outlet. (b) Expanded cross-section of filter wall thickness, L_T. (c) Cross-sectional SEM image of microstructure comprising the filter wall.

particle composites, employing the lattice Boltzmann (LB) method, which is well-known to be relatively effective in handling complex geometrical shapes [26,27]. The porous structures are constructed by regularly or randomly placing individual spherical particles for making regular simple cubic (SC) and face-center cubic (FCC) structures or a random (R) structure and by overlapping them for making overlapped-random (OR) structure. Especially, the OR structure corresponds to the geometry of the actual ceramic filter realized through the sintering process of Mg-Al silicate particles. From the comparison of results of our LB simulations and existing models in the literature according to the change in porosity, representative key variables for predicting permeability were revealed: porosity, tortuosity, and effective pore-throat radius. In particular, a modified capillary model was proposed to practically and reasonably quantify the permeability by assembling above key variables reflecting more complex porous characteristics at low porosity.

THEORETICAL BACKGROUND AND SIMULATION METHOD

1. Permeability and Tortuosity of Porous Media

According to Darcy's law, the gas flux (Q) penetrating the filter is proportional to the wall pressure drop (ΔP) and inversely proportional to the fluid dynamic viscosity (μ), as follows [28]:

$$Q = -\frac{K\Delta P}{\mu L_T}. \quad (1)$$

Here, the permeability (K) is generally expressed as a function of porosity (ϕ) [15,16,25].

The Kozeny-Carman model (K-C model, Eq. (2)) for describing the permeability was originally based on the simple capillary model for the pore networks by Kozeny [15] and further improved by Carman [16] considering the tortuosity (T) written as

$$K = \frac{\phi R_H^2}{C_{KC} T^2}, \quad (2)$$

where $R_H=\phi/S_v(1-\phi)$ is the hydraulic radius of voids and pores and S_v is the specific surface area defined as the total surface area of voids and pores per the solid volume. C_{KC} is the Kozeny-Carman coefficient, demonstrating that its constant value of 5 has been a reasonable approximation for beds of granular materials [16,29]. In addition, Happel [29,30] proposed a theoretical equation for the K-C constant using a cell model applicable over a wide porosity range. However, the Happel cell (H-C) model has been known to show some discrepancy with experimental results at low porosity (ϕ<0.2) and for porous media composed of non-spherical particles [30].

In particular, the hydraulic tortuosity $T=\langle\lambda\rangle/L_T$ [16] for reflecting the non-simple tortuous flow path is the ratio between the average length ($\langle\lambda\rangle$) of the actual flow path and the simplified straight length of the flow path parallel to the pressure drop direction (L_T), where $\langle\cdots\rangle$ represents the ensemble average. For example, T in the simplest case of the spherical granular bed is reduced to $\sqrt{2}$ [16,31]. However, the tortuosity generally changes with the varying porosity, especially at low porosity [31]. Table 1 shows the representative models related to porosity and tortuosity in the form of logarithmic or power-law functions for porous media flow systems assembled from spherical particles. Two of them deserve mention here. Mota et al. [32] experimentally obtained the porosity-tortuosity relation based on binary mixtures of spherical particles and Ahmadi et al. [33] showed theoretical tortuosity values using a mathematical model for a porous medium regularly aligned by monodisperse spheres. However, there is a difference between the tortuosity predicted by the proposed models and the measured value from porous materials composed of various particle shapes [31,34-36]. Numerical approaches have been proposed to accurately calculate hydraulic tortuosity using the velocity field in arbitrary porous regions [36], as will be explained in Section 3-2.

2. Key Variables Characterizing Permeability in the Capillary Model

The grains for various sizes and shapes appearing in actual porous media such as ceramic filters can be characterized through C_{KC} of the K-C model. However, the structures of substantially irregular grains through the sintering process with low porosity are rarely

Table 1. Some hydraulic tortuosity models in the literature

Model equation		Porous geometry	Reference
$T \approx \sqrt{2}$		Cubic packing of equal-sized spheres	Carman [16]
$T = 1 - p\ln\phi$, p=0.49		High porosity beds (spheres and fibers)	Mauret and Renaud [37]
$T = \phi^{-p}$, p=0.4		Binary mixture of spherical particles	Archie [38] Mota et al. [32]
$T = \sqrt{\frac{2\phi}{3[1-p(1-\phi)^{2/3}]} + \frac{1}{3}}$	p=1.209	Mono-sized spheres (Cubic packing)	Ahmadi et al. [33]
	p=1.108	Mono-sized spheres (Tetrahedral packing)	

reflected in this model. Considering the difficulty of investigating complex-structured porous media with low porosity using the conventional models, models incorporating the structural properties of pores and voids inside porous media were designed [39].

At moderate and low porosity, the structures of voids and pores are simplified to a bundle of capillary tubes similar to the simple capillary model by Kozeny [15,16,39]. In such a modified capillary model, the gas flux is proportional to the cross-sectional area of the cylinder-shaped capillary tube, and inversely proportional to the capillary length [39]. The cross-sectional area of a single pore channel can be simplified to πR_H^2 and the actual travel distance of a fluid element flowing through the tortuous path is reflected by the tortuosity. In addition, the variation of cross-sectional area of pore channel along the flow path is considered by introducing a constriction factor (C) [40,41], which is representatively defined as the ratio of the maximum and minimum cross-sectional areas [42].

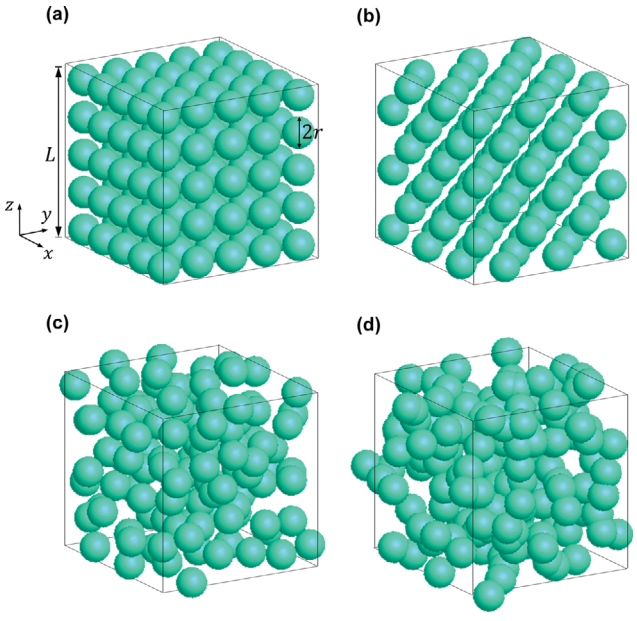

Fig. 2. Schematic images of porous geometry at $\phi \approx 0.7$ and L/r=12: (a) Simple cubic array (SC), (b) face-centered cubic array (FCC), (c) random array (R), and (d) overlapped random array (OR). L is the length of cubic box, r is the radius of spherical particles, and the average grain size in the cubic box, $R_{Grain}=\langle r \rangle$. For example, R_{Grain} is evaluated as r for (a)-(c) and 0.95r for (d).

The K-C coefficient of Eq. (2) was theoretically determined to be $C_{KC}=8C$ from the previous study [39]. Thus, the permeability based on the modified capillary model was correlated with structural properties of R_H, C, T, and ϕ.

3. Numerical Simulation Using Lattice Boltzmann Method

3-1. Simulation Conditions

In this study, the regular and irregular porous materials are composed of spherical particles with a radius of r in a cubic box with periodic boundaries of length L in the x, y, and z directions, as displayed in Fig. 2. In the SC, FCC, and R structures, the average particle size of media ($R_{Grain}=\langle r \rangle$) is the size of spherical particles, i.e., $R_{Grain}=r$. However, in the OR structure constructed by monodispersed spherical particles, R_{Grain} is evaluated as $L^3\sqrt{\frac{3\phi}{4\pi N}}$. N is the total number of particles in the periodic box, which controls the overlapped degree [14].

To first confirm whether L/r of numerically generated porous samples is sufficiently large to acquire meaningful bulk porous properties, the representative volume element (RVE) analysis for the distributions of pore size or surface area was adopted [43,44]. As shown in Fig. 3, sizes of individual pores are classified through the algorithm of Rabbani et al. [45], where the pore radius, r_H is defined as the radius of a circle with a cross-sectional area equivalent to that of each pore, and average pore radius of the entire porous medium is $R_H=\langle r_H \rangle$. In addition, the surface area of each sample was calculated using the marching cube algorithm [46]. The RVE analysis uses the relative standard deviation (RSD), i.e., the standard deviation divided by the average of each property, for the relative comparison of $\langle r_H \rangle$ and surface area distributions from ten samples under constant porosity condition. In this study, L/r was chosen to have the RSD less than 3%.

3-2. Flow Simulation Using the Lattice Boltzmann Method

The Newtonian fluid flow-through various porous media as shown in Fig. 2 is governed by the following hydrodynamic equations:

$$\frac{\partial \rho}{\partial t} + \nabla \cdot (\rho \mathbf{u}) = 0, \tag{3}$$

$$\rho\left(\frac{\partial \mathbf{u}}{\partial t} + \mathbf{u} \cdot \nabla \mathbf{u}\right) = -\nabla p + \nabla \cdot \boldsymbol{\sigma} + \mathbf{f}_{ext}, \tag{4}$$

where ρ is the fluid density, $\mathbf{u}$ is the fluid velocity, p is the pressure, $\boldsymbol{\sigma}$ is the viscous stress, and $\mathbf{f}_{ext}$ is the external force density driving the fluid flow. The surface of particles constituting the

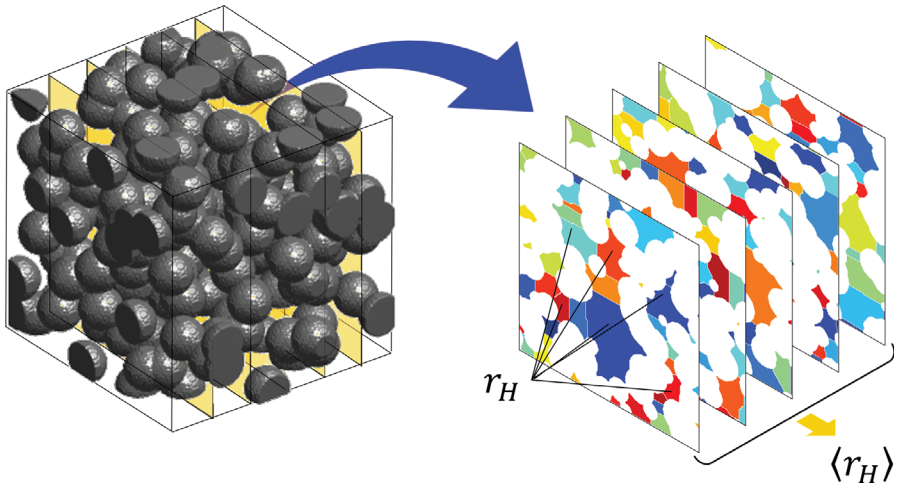

Fig. 3. Several cross-sections of an OR-structured sample (ϕ=0.20) whose pores are determined by Rabbani et al. algorithm [45]. Each pore is represented by a different color.

porous media satisfies the no-slip boundary condition. These equations were solved by the LB-based SUSP3D code [47-50].

The LB method divides the physical space and the velocity space into uniformly spaced grids [47]. The hydrodynamic variables are expressed through the discretized velocity distribution function, n_i. Time evolution of n_i is expressed as follows:

$$n_i(\mathbf{x}+\mathbf{c}_i\delta_t, t+\delta_t)=n_i(\mathbf{x}, t)+\sum_{j=0}^{b}\mathcal{L}_{ij}(n_i(\mathbf{x}, t)-n_i^{eq}(\mathbf{x}, t)), \quad (5)$$

where $\mathbf{x}$ is the position vector, $\mathbf{c}_i$ is the fluid velocity vector along the i direction in discrete time, t, δ_t is the time step, and $\mathcal{L}_{ij}$ is the linearized collision operator. Also, indices (i or j) have values from 0 to b (b=18 for the D3Q19 model). Equilibrium distribution function is provided as follows:

$$n_i^{eq}=a^{c_i}\rho\left[1+\frac{\mathbf{c}_i\cdot\mathbf{u}}{c_s^2}+\frac{(\mathbf{c}_i\cdot\mathbf{u})^2}{2c_s^2}-\frac{\mathbf{u}^2}{2c_s^2}\right]. \quad (6)$$

The weighting factor, a^{c_i} is a^0=1/3, a^1=1/18, and $a^{\sqrt{2}}$=1/36 according to the three levels of speed, c_i=0, 1, and $\sqrt{2}$, respectively, in the D3Q19 model. The speed of sound in lattices is $c_s^2=c^2/3$ with $c=\delta/\delta_t$. δ is the length of the interval between lattices. The fluid density and the momentum, $\rho\mathbf{u}$, expressed through n_i are defined, as shown below:

$$\rho=\sum_{j=0}^{b}n_j,\ \rho\mathbf{u}=\sum_{j=0}^{b}c_jn_j. \quad (7)$$

The two-relaxation time (TRT) model was used as the collision operator, and the fluid viscosity was expressed in Eq. (8):

$$\mu=\rho c_s^2\delta_t\left(\tau-\frac{1}{2}\right), \quad (8)$$

by using one of two relaxation times, τ. Note that the other relaxation time can be chosen to reduce the numerical error when applying a no-slip boundary on the solid surface [51,52]. In addition, from the velocity field obtained by LB method, the hydraulic tortuosity is directly calculated as follows:

$$T=\frac{\langle|\mathbf{u}|\rangle}{\langle u_x\rangle}, \quad (9)$$

where $|\cdots|$ is the velocity magnitude, and u_x denotes the velocity component along the applied pressure gradient represented by $\mathbf{f}_{ext}$.

RESULTS AND DISCUSSION

1. Permeability in Porous Media with Non-overlapped and Overlapped Spherical Particles

In Fig. 4, the dimensionless permeability, $\tilde{K}=K/R_{Grain}^2$, obtained from LB simulations is plotted against the porosity for porous media with non-overlapped (SC, FCC, and R) and overlapped (OR) spheri-

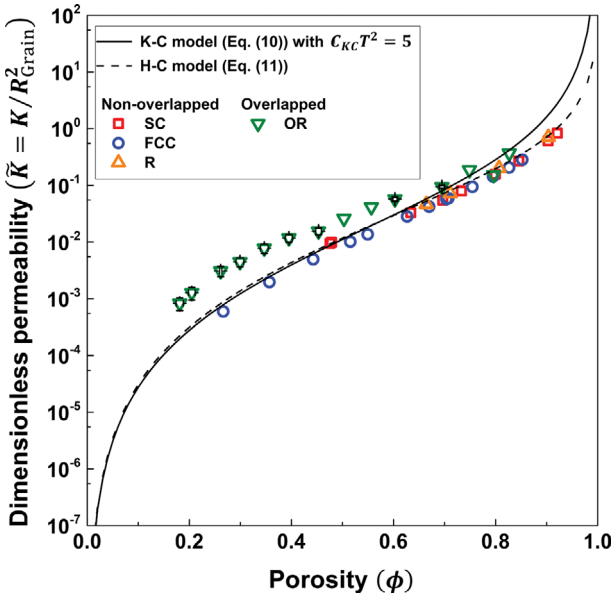

Fig. 4. Dimensionless permeability data for porous media with non-overlapped and overlapped porous structure at different ϕ values. The LB results (symbols) are compared with the K-C model with $C_{KC}T^2$=5 (Eq. (10)) and the H-C model (Eq. (11)).

cal particles. The K-C model of Eq. (2) was modified to express the dimensionless permeability as follows:

$$\tilde{K} = \frac{\phi^3}{9C_{KC}T^2(1-\phi)^2}. \quad (10)$$

The following H-C model [30] was also considered here to compare permeability data:

$$\tilde{K} = \left[\frac{6-9\phi^{1/3}+9\phi^{5/3}-2\phi^2}{9\phi(3+2\phi^{5/3})}\right]. \quad (11)$$

The K-C model with $C_{KC}T^2=5$ [16] and the H-C model are well suited for LB simulation results for non-overlapped geometry.

As shown in Fig. 4, the permeability results from LB simulations are divided into two groups. Both non-overlapped SC, FCC, and R structures tended to have a good agreement with both the K-C with $C_{KC}T^2=5$ and the H-C models, indicating that the particle arrangement by such non-overlapped structures did not affect the permeability for corresponding porous media. Note that over large porosity condition (ϕ>0.6), the H-C model better agreed with simulation results than the K-C model. However, the porous media with the OR structure showed different tendency in permeability from cases with non-overlapped structures. In the OR-structured case, the permeability deviates from the K-C or H-C model when $\phi \leq 0.6$, especially at low porosity, due to its rather complex pore structure with some dead zones and closed pores. Note that the value of $C_{KC}T^2$ in the K-C model should be empirically determined for actual porous structures.

To suitably characterize the permeability of complex (i.e., OR-structured) porous media with low porosity, it is important to define key structural parameters by focusing on the shapes of voids and pores instead of the grains, as described in the next sections.

2. Hydraulic Radius and Constriction Factor

As described in Section 2.2 for the modified capillary model, the fluid flowing through the actual pore geometries composed of

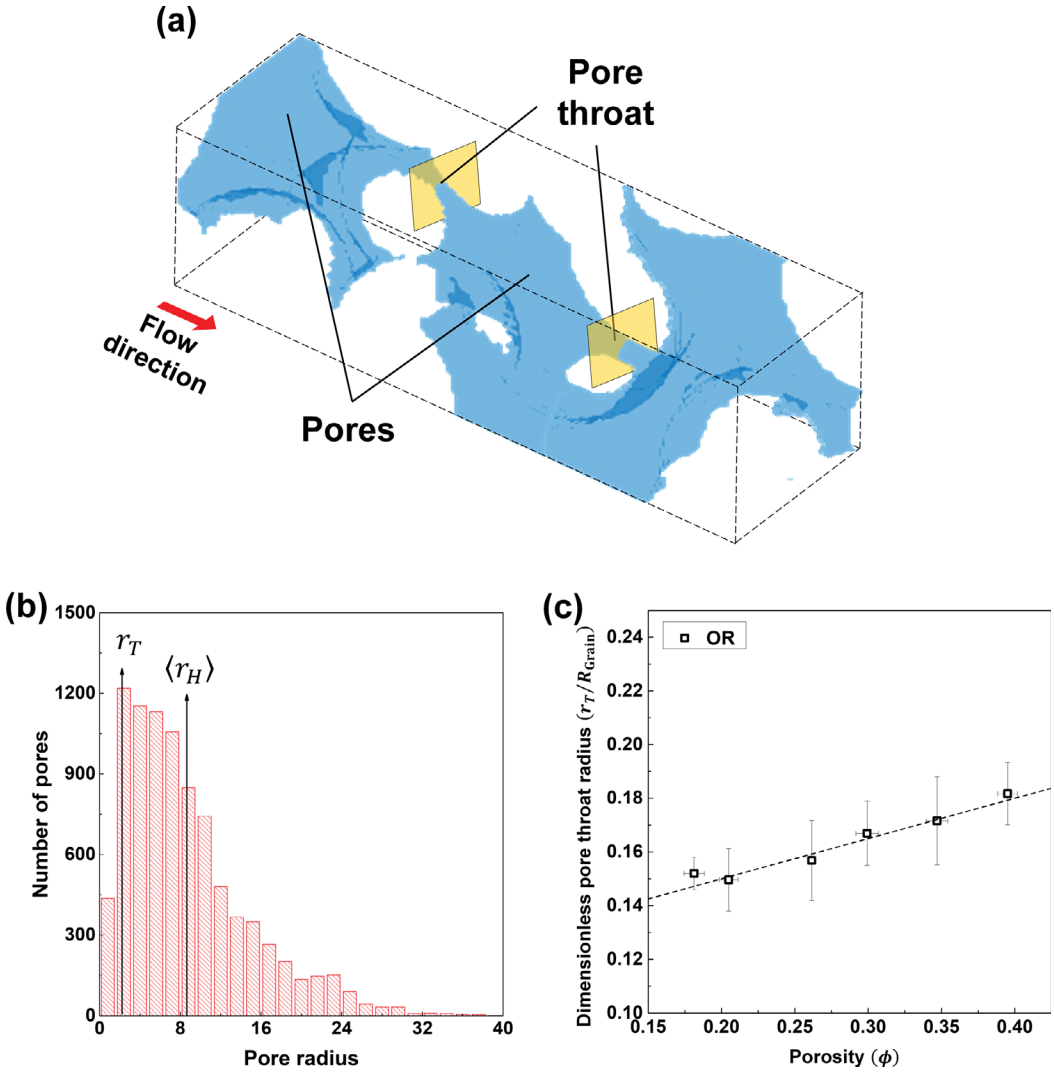

Fig. 5. (a) Schematic image of pore geometry in OR-structured media; pore throat with very small cross-section is the connection point between the pores and voids. (b) Illustration of pore radius distribution for OR-structured medium with ϕ=0.30 in lattice unit; r_T represents the lower 15% of pore size distribution. (c) The relation of porosity and pore throat radius; the dotted line with Eq. (13) fits LB simulation data for OR-structured media.

connected pores and voids experiences varying cross-sectional area along the flow path; in particular, it may penetrate a very small cross-sectional area, the so-called pore throat. Note that a pore throat can be only defined in the porous region of low porosity where capillary-shaped passages can be realized. As portrayed in Fig. 5(a), the pore throat connects the pores and voids, which significantly affects the overall flow rate. The constriction factor, C can be expressed as the ratio of the average cross-sectional area of the entire porous system to the average cross-sectional area at the pore throat as follows [42]:

$$C=\frac{\langle r_H\rangle^2}{r_T^2}, \tag{12}$$

where r_T was selected here around the lower 15% of pore radius distribution (Fig. 5(b)), considering the possibility of isolated spaces and clogged pathways. The relation between average pore throat radius and porosity is presented in Fig. 5(c), which exhibits monotonically increasing r_T/R_{Grain} with respect to the porosity, based on the following linear form:

$$\frac{r_T}{R_{Grain}}=0.12+0.15\phi \tag{13}$$

Using Eq. (12) in the modified capillary model, it can be seen that the structural parameter r_T plays a key role in evaluating the permeability in complex porous media of low porosity, as substantiated in Section 4 of Results and Discussion.

3. Tortuosity of Porous Media

Fig. 6 shows the relation between porosity and tortuosity for various porous media with nonoverlapped (FCC and R) and overlapped (OR) structures in the Darcy flow regime. Tortuosity varies in the range of 1 and 2 under the given porosity conditions, monotonically decreasing as the porosity increases. Two tortuosity models by Mota et al. [32] and Admadi et al. [33], as mentioned in Section 2.2, are indicated by solid and dotted black lines, respectively, in Fig. 6, which are roughly upper and lower bounds of the LB simulation results, except under low porosity condition. However, the LB results show different trends in comparison to two models, depending on the grain structure. The cases with FCC and R structures composed of non-overlapped spheres showed good agreement with the Ahmadi et al's model. For the OR-structured case, the tortuosity data by LB simulations were consistent with Mota et al's model in high porosity region (ϕ>0.6), similarly following Ahmadi *et al.*'s model in the low porosity region (ϕ<0.3, after the transition in the moderate porosity region of ϕ=0.3−0.6.

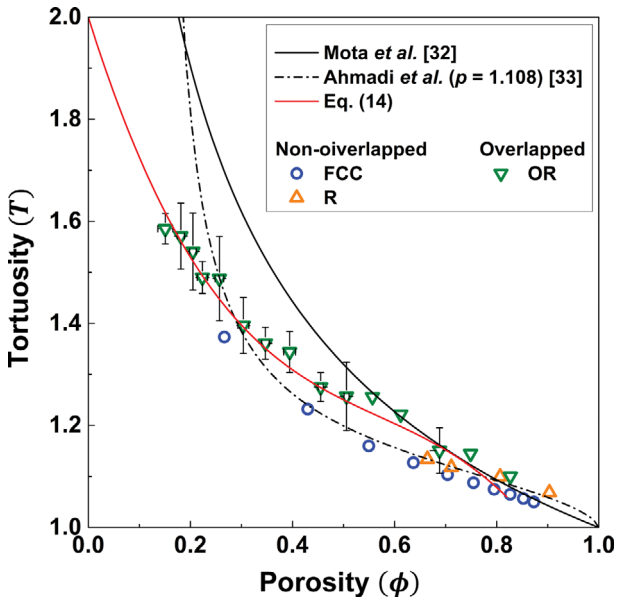

Fig. 6. Tortuosity data (symbols) of porous media with non-overlapped (FCC and R) and overlapped (OR) structures obtained from LB simulations. The lines represent the empirical model by Mota et al. [32], the analytical model by Ahmadi et al. [33], and the curve-fitting cubic equation of LB results for OR-structured media (Eq. (14)).

The different tortuosity pattern of the OR case may be due to the structure with broad pore size distribution constructed by arbitrarily-overlapped spheres, distorting the flow path more than the other structure cases made by nonoverlapped monodisperse spheres. The pore size distribution in the OR case at high porosity would be similar to that by Mota et al. based on a mixed system composed of binary particles. As the porosity decreases, its pore size distribution becomes narrower and is analogous to those by the other structures. The trend of tortuosity in the OR structure was formulated by fitting the LB results in a following cubic function:

$$T=2-3.2\phi+4.8\phi^2-2.8\phi^3. \tag{14}$$

This relation can be used to predict the tortuosity of the OR-structured case in a wide range of porosity.

4. Prediction of Permeability with Porosity, Pore Throat Radius, and Tortuosity

As explained in Section 2.2, the K-C model can be changed to the modified capillary model using rearranging structural parameters, R_H, C, T, and ϕ of the porous media. Eq. (2) is written as:

$$K=\frac{\phi R_H^2}{CT^2}, \tag{15}$$

by introducing C instead of C_{KC}. Using the relation of C in Eq. (12), Eq. (15) is further simplified in the following relation:

$$K=\frac{\phi r_T^2}{T^2}, \tag{16}$$

where the permeability is a simple function of three structural parameters, ϕ, r_T, and T.

Fig. 7 compares the dimensionless permeability data for OR-structured porous media obtained from LB simulations and several models including Eq. (16) in the low porosity region of $\phi\leq$0.4. The permeability by Eq. (16) incorporating r_T/R_{Grain} from Eq. (13) and T from Eq. (14) is satisfactorily analogous to the LB simulation results at low porosity, compared to the H-C and K-C models. This means that the structural parameters, ϕ, r_T, and T, well reflect the structural features of the pores and voids in the low porosity region. Consequently, our model of Eq. (16) can be usefully applied to properly quantify the permeability in complex porous media with low porosity, composed of sintered grains such as OR structures.

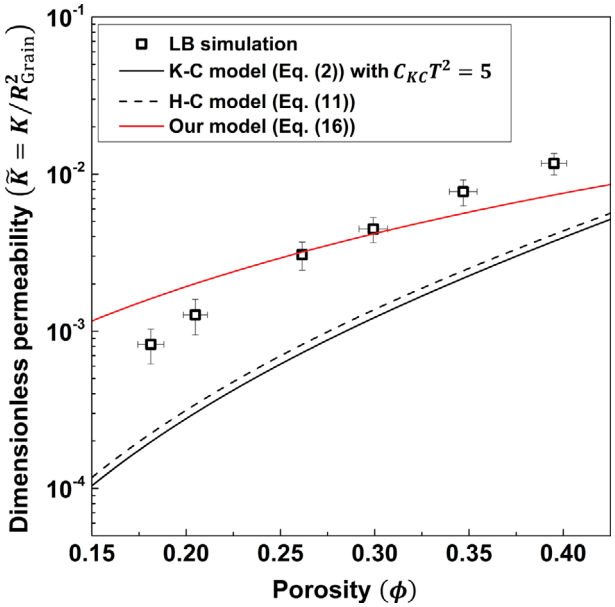

Fig. 7. Comparison of permeability data of OR-structured porous media from LB simulation and different models in lattice unit. The solid line represents the K-C model (Eq. (2)) with $C_{KC}T^2$=5, the dotted line is the H-C model (Eq. (11)), and the red line is Eq. (16) using r_T/R_{Grain} from Eq. (13) and T from Eq. (14). Symbols are the LB simulation data.

CONCLUSION

The effect of structural property on the Darcy flow in the porous media composed of non-overlapped (SC, FCC, and R structures) and overlapped (OR structure) grains was investigated using the LB method. In particular, an OR-structured porous system of low porosity similar to that of an actual sintered ceramic filter was mainly the focus here. The size of the porous structure used in the simulation was reasonably determined via the RVE analysis using distributions of pore size and surface area. Permeability data of the SC, FCC, and R structures, evaluated from LB simulation, showed good agreement with the K-C and H-C models. However, the permeability results of the OR structure significantly differed from these models under low porosity conditions. Based on a modified capillary model, key structural variables affecting permeability of complex-structured porous media were found: porosity, tortuosity, and pore-throat radius. Relations of tortuosity and pore-throat radius with respect to porosity were newly established by fitting LB simulation data for OR structure, respectively. A practical model combining above-mentioned structural variables was newly derived through modification of the Kozeny-Carman model, which shows a good agreement with LB simulation data and thus could reasonably estimate the permeability of porous media with low porosity.

ACKNOWLEDGEMENTS

This study was supported by the Ministry of Trade, Industry, and Energy (MOTIE, Korea) under the Industrial Technology Innovation Program (No. 20011712) and by National Research Foundation of Korea (NRF) grants funded by the Ministry of Science and ICT (MSIT) of the Korean government (No. NRF-2016R1A5A1009592 and NRF-2021M3H4A6A01041234).

CONFLICT OF INTEREST

The authors have no conflict of interest to declare.

REFERENCES

1. U. D. Schiller and F. Wang, *MRS Commun.*, **8**, 358 (2018).
2. D. Fino, P. Fino, G. Saracco and V. Specchia, *Korean J. Chem. Eng.*, **20**, 445 (2003).
3. S. Bensaid, D. L. Marchisio, D. Fino, G. Saracco and V. Specchia, *Chem. Eng. J.*, **154**, 211 (2009).
4. T.-T. Nguyen, A. Demortière, B. Fleutot, B. Delobel, C. Delacourt and S. J. Cooper, *npj Comput. Mater.*, **6**, 1 (2020).
5. M. F. Lagadec, R. Zahn and V. Wood, *Nat. Energy*, **4**, 16 (2019).
6. G. Jeon, S. Y. Yang and J. K. Kim, *J. Mater. Chem.*, **22**, 14814 (2012).
7. M. Masoudi, A. G. Konstandopoulos, M. S. Nikitidis, E. Skaperdas, D. Zarvalis, E. Kladopoulou and C. Altiparmakis, *SAE Transactions*, **110**, 650 (2001).
8. C. J. Kamp, P. Folino, Y. Wang, A. Sappok, J. Ernstmeyer, A. Saeid, R. Singh, B. Kharraja and V. W. Wong, *SAE Int. J. Fuels Lubr.*, **8**, 487 (2015).
9. G. A. Merkel, W. A. Cutler, T. Tao, A. Chiffey, P. Phillips, M. V. Twigg and A. Walker, in Proceedings of the 9th Diesel Engine Emissions Reduction Conference (2003).
10. M. Nakamura, K. Yokota, M. Hattori and M. Ozawa, *SAE Technical Paper Series*, 2020-01-2169 (2020).
11. O. A. Haralampous, I. P. Kandylas, G. C. Koltsakis and Z. C. Samaras, *Int. J. Engine Res.*, **5**, 149 (2004).
12. R. H. Perry, *Perry's chemical engineers' handbook*, McGraw-Hill, New York (1984).
13. R. C. Reid, J. M. Prausnitz and B. E. Poling, *The properties of gases and liquids*, McGraw-Hill, New York (1987).
14. D. Y. Lee, G. W. Lee, K. Yoon, B. Chun and H. W. Jung, *Appl. Surf. Sci.*, **429**, 72 (2018).
15. J. Kozeny, *Sitzungsber. Akad. Wiss. Wien*, **136**, 271 (1927).
16. P. C. Carman, *Trans. Inst. Chem. Eng.*, **15**, 150 (1937).
17. F. Civan, *Reservoir formation damage*, Gulf Professional Publishing, Burlington, MA (2007).
18. M. Safari, R. Gholami, M. Jami, M. A. Ananthan, A. Rahimi and W. S. Khur, *J. Pet. Sci. Eng.*, **205**, 108896 (2021).
19. A. Nabovati, E. W. Llewellin and A. C. M. Sousa, *Compos. Pt. A-Appl. Sci. Manuf.*, **40**, 6 (2009).
20. F. Wang and U. D. Schiller, *Phys. Rev. Mater.*, **4**, 083803 (2020).
21. F. Wang and U. D. Schiller, *Phys. Rev. Mater.*, **4**, 083804 (2020).
22. X. Garcia, L. T. Akanji, M. J. Blunt, S. K. Matthai and J. P. Latham, *Phys. Rev. E.*, **80**, 021304 (2009).
23. P. Guo, *Transp. Porous Media*, **95**, 285 (2012).
24. C. Tien and B. V. Ramarao, *Powder Technol.*, **237**, 233 (2013).
25. R. Schulz, N. Ray, S. Zech, A. Rupp and P. Knabner, *Transp. Porous Media*, **130**, 487 (2019).
26. S. Chen and G. D. Doolen, *Annu. Rev. Fluid Mech.*, **30**, 329 (1998).
27. S. Succi, E. Foti and F. Higuera, *Europhys. Lett.*, **10**, 433 (1989).

28. H. Darcy, *Les fontaines publiques de la ville de Dijon*, V. Dalmont, Paris (1856).
29. J. Happel and H. Brenner, *Low Reynolds number hydrodynamics: With special applications to particulate media*, Springer, Berlin (2012).
30. J. Happel, *AIChE J.*, **4**, 197 (1958).
31. B. Ghanbarian, A. G. Hunt, R. P. Ewing and M. Sahimi, *Soil Sci. Soc. Am. J.*, **77**, 1461 (2013).
32. M. Mota, J. A. Teixeira, W. R. Bowen and A. Yelshin, *Trans. Filt. Soc.*, **1**, 101 (2001).
33. M. M. Ahmadi, S. Mohammadi and A. N. Hayati, *Phys. Rev. E*, **83**, 026312 (2011).
34. A. Koponen, M. Kataja and J. Timonen, *Phys. Rev. E*, **54**, 406 (1996).
35. M. Matyka, A. Khalili and Z. Koza, *Phys. Rev. E*, **78**, 026306 (2008).
36. A. Duda, Z. Koza and M. Matyka, *Phys. Rev. E*, **84**, 036319 (2011).
37. E. Mauret and M. Renaud, *Chem. Eng. Sci.*, **52**, 1807 (1997).
38. G. E. Archie, *Trans. AIME*, **146**, 54 (1942).
39. C. F. Berg, *Transp. Porous Med*, **103**, 381 (2014).
40. F. A. L. Dullien, *Porous media: Fluid transport and pore structure*, Academic Press, New York (1992).
41. C. F. Berg, *Phys. Rev. E*, **86**, 046314 (2012).
42. E. E. Petersen, *AIChE J.*, **4**, 343 (1958).
43. X. Huang, Q. Wang, W. Zhou, D. Deng, Y. Zhao, D. Wen and J. Li, *Powder Technol.*, **283**, 618 (2015).
44. E. Brun, J. Vicente, F. Topin, R. Occelli and M. J. Clifton, *Adv. Eng. Mater.*, **11**, 805 (2009).
45. A. Rabbani, S. Jamshidi and S. Salehi, *J. Pet. Sci. Eng.*, **123**, 164 (2014).
46. W. E. Lorensen and H. E. Cline, *ACM SIGGRAPH Computer Graphics*, **21**, 163 (1987).
47. A. J. C. Ladd, *J. Fluid Mech.*, **271**, 285 (1994).
48. A. J. C. Ladd and R. Verberg, *J. Stat. Phys.*, **104**, 1191 (2001).
49. N. Q. Nguyen and A. J. C. Ladd, *Phys. Rev. E*, **66**, 046708 (2002).
50. B. Chun, J. S. Park, H. W. Jung and Y.-Y. Won, *J. Rheol.*, **63**, 437 (2019).
51. B. Chun and H. W. Jung, *Phys. Fluids*, **33**, 053318 (2021).
52. I. Ginzburg and D. d'Humieres, *Phys. Rev. E*, **68**, 066614 (2003).